Peer-reviewed version available at Condens. Matter 2018, 3, 27; doi:10.3390/condmat3030027

Article

Dependency of Charge-Discharge Rate on Lithium Reaction Distributions for a Commercial Lithium Coin Cell Visualized by Compton Scattering Imaging

Kosuke Suzuki [1,*], Ryo Kanai [1], Naruki Tsuji [2], Hisao Yamashige [3], Yuki Orikasa [4], Yoshiharu Uchimoto [5], Yoshiharu Sakurai [2] and Hiroshi Sakurai [1]

[1] Graduate School of Science and Technology, Gunma University, Kiryu, Gunma 376-8515, Japan; t161d023@gunma-u.ac.jp; sakuraih@gunma-u.ac.jp
[2] Japan Synchrotron Radiation Research Institute (JASRI), SPring-8, Sayo, Hyogo 679-5198, Japan; ntsuji@spring8.or.jp; sakurai@spring8.or.jp
[3] Material Platform Engineering Division, Toyota Motor Corporation, Toyota, Aichi 471-8572, Japan; hisao_yamashige@mail.toyota.co.jp
[4] Department of Applied Chemistry, Ritsumeikan University, Kusatsu, Shiga 525-8577, Japan; orikasa@fs.ritsumei.ac.jp
[5] Graduate School of Human and Environmental Studies, Kyoto University, Sakyo, Kyoto 606-8501, Japan; uchimoto.yoshiharu.2n@kyoto-u.ac.jp
* Correspondence: kosuzuki@gunma-u.ac.jp; Tel.: +81-277-30-1714

Abstract: In this study, lithium reaction distributions, dependent on charge-discharge rate, were nondestructively visualized for a commercial lithium-ion battery, using the Compton scattering imaging technique. By comparing lithium reaction distributions obtained from two different charge-discharge speeds, residual lithium ions were detected at the center of the negative electrode on a fully discharged state, by relatively high-speed discharge rate. Moreover, we confirmed that inhomogeneous reactions were facilitated on a relatively high-speed charge-discharge rate, in both the negative and positive electrodes. A feature of our technique is that it can be applied to commercially used lithium-ion batteries, because it uses high-energy X-rays with a high penetration power. Our technique thus opens a novel analyzing pathway for developing advanced batteries.

Keywords: lithium reaction distribution; in-operando measurement; Compton scattering imaging

1. Introduction

Although lithium-ion rechargeable batteries are widely used in our lives, their demand is rapidly increasing, since the development of electric vehicles is attracting much attention all over the world. To further expand the use of electric vehicle, not only high capacities, but also high safety and long lifetimes are required for the batteries. Moreover, people expect fast-charging batteries at a similar refueling speed as in the gasoline car. However, in a previous neutron diffraction study, it was reported that inhomogeneous reactions occur in the graphite negative electrode at a high-speed charge-discharge rate [1]. These inhomogeneous reactions are related to the degradation of the battery performance; furthermore, they carry some great risks. Therefore, it is important to monitor lithium reactions directly in the batteries on *in-situ* or *in-operando* conditions. Although the neutron diffraction technique being a powerful tool for *in-operando* measurement, it reveals the reaction mechanism through the change of the lattice parameter in the electrode materials.

Recently, we have been developing a method for directly monitoring lithium ions using high-energy X-ray Compton scattering technique, called Compton scattering imaging [2-4]. This

Peer-reviewed version available at Condens. Matter 2018, 3, 27; doi:10.3390/condmat3030027

technique enables us to measure the reactions in the batteries under *in-situ* and *in-operando* conditions because it uses high-energy X-rays as an incident beam, which has high-penetration power in the materials [5]. Moreover, a line-shape of Compton scattered energy spectrum, called Compton profile, is obtained from this incoherent scattering technique and depends on the element. Here, the Compton profile, $J(p_z)$, is shown in the following equation [6],

$$J\left(p_z\right)=\iint \rho\left(\mathbf{p}\right)dp_x dp_y \quad , \tag{1}$$

where $\rho(\mathbf{p})$ is the electron momentum density, $\mathbf{p} = (p_x, p_y, p_z)$ is the momentum, and p_z is assumed to lie along the direction of the scattering vector. The $\rho(\mathbf{p})$ is expressed by the following [7,8],

$$\rho\left(\mathbf{p}\right)=\sum_j n_j\left|\int \Psi_j\left(\mathbf{r}\right)\exp\left(-i\mathbf{p}\cdot\mathbf{r}\right)d\mathbf{r}\right|^2 \quad , \tag{2}$$

where $\Psi_j(\mathbf{r})$ is the wavefunction of an electron in the j-state and n_j is the electron occupation. The index j covers all constituent atoms and orbitals. Since the Compton profile is directly linked to the wavefunction of the electrons, its line-shape of varies depending on each element. So far, we have demonstrated a method to quantify the lithium concentration from the change of the line-shape of the Compton profile (Shape parameter analysis; *S*-parameter) [3] and have successfully determined simultaneously lithium compositions at the positive and negative electrodes during a charge-discharge cycle [4]. Along with others, we have studied the mechanism of electrode reactions in positive electrode materials, $Li_xMn_2O_4$, Li_xCoO_2, and Li_xFePO_4, using Compton profiles [9-11].

In this study, we visualize lithium reaction distributions on two different charge-discharge speed by applying Compton scattering imaging to commercial lithium-ion coin cell of VL2020 and discuss the change of the reactions depending on the charge-discharge speed.

2. Experimental study

The Compton scattering experiment was performed with a 08 W high-energy X-ray beamline of SPring-8, Japan. The experimental configuration was the same as our previous in-operando measurement of lithium concentration [4]. The incident X-ray energy was 115.56 keV, and the scattering angle was fixed at 90°. Compton-scattered energy spectrum was measured by nine segments of pure Ge solid-state detector. The proving volume of a sample was limited by an incident slit and a collimator slit, which was arranged between the sample and detector. The size of the incident and collimator slits were 25 μm in height, 500 μm in width, and 500 μm in diameter, respectively. Hence, the observing region was 25 μm in height, 500 μm in width, and 500 μm in depth. A sample was set on a movable stage along the x, y and z directions. The sample was a commercial coin-type lithium-ion rechargeable battery VL2020, made by Panasonic Corporation. This battery had a diameter of 20 mm and a 2 mm thickness; it was composed of V_2O_5 positive electrode (800 μm in thickness), LiAl alloy negative electrode (300 μm in thickness), olefin-based nonwoven fabric separator, Al wire-netting spacer, and dimethoxyethane electrolyte. The state of charge (SOC) of the batteries was controlled by two charge-discharge rates, 1C and 0.2C. Here, 1C and 0.2C denote that the time between a fully discharged state and a fully charged state is 1 h and 5 h, respectively. The Compton scattering energy spectrum was measured by changing the vertical and horizontal positions of the sample with respect to the incident X-rays mapping the lithium reaction distribution.

The obtained Compton scattered energy spectra were transformed to *S*-parameters. The *S*-parameter digitalizes the line-shape of a Compton scattered energy spectrum. As mentioned above, the line-shape of the Compton scattered energy spectrum changes through the elements, because the Compton profile reflects the electron momentum density distributions. The *S*-parameter is directly linked to lithium concentration in the positive and negative electrodes. Here, the lithium momentum density is distributed at low momentum regions; thus, the high *S*-parameter value

Peer-reviewed version available at Condens. Matter 2018, 3, 27; doi:10.3390/condmat3030027

corresponds to a high lithium concentration [12]. The *S*-parameter is defined through the following equations [3,4],

$$S = \frac{S_L}{S_H} = \frac{\int_{-1}^{1} J(p_z)\,dp_z}{\int_{-5}^{-1} J(p_z)\,dp_z + \int_{1}^{5} J(p_z)\,dp_z}, \quad (3)$$

where S_L and S_H are the areas under the Compton profile covering the low- and high-momentum regions; parameters of ±5 and ±1 are the ranges within the low- and high-momentum regions, respectively. In this study, analysis of lithium reaction distributions and lithium concentrations, dependent on the charge-discharge rate, were conducted through the *S*-parameters.

3. Results and Discussion

Figure 1(a) shows the entire internal structure of the sample coin cell through *S*-parameters. In this figure, the region of vertical position z < -0.1 mm and z >1.4 mm corresponds to the battery outer stainless steel case (SUS), region around z = 0 mm corresponds to the spacer, region 0.1 < z < 0.35 mm corresponds to LiAl negative electrode, region 0.4 < z < 0.55 mm corresponds to the separator, and 0.6 < z < 1.3 mm corresponds to the V_2O_5 positive electrode. To study the details of the lithium reaction, we measured the Compton scattered energy spectrum precisely at the region of 0 < z < 0.7 mm. Figure 1(b) shows the variation of the *S*-parameters in the full-discharged state (SOC0) and full-charged state (SOC100) when the battery is charged and discharged by 0.2C. By charging the battery, the *S*-parameters increase by about 1.7 % at the negative electrode; on the other hand, they decrease by about 1.8 % at the positive electrode. Moreover, the separator position shifts toward the positive electrode direction by charging the battery. This means that the lattice volume of the negative electrode material expanded through the insertion of lithium ions. From the above, the *S*-parameter allow us to study lithium reaction distributions in the coin cell.

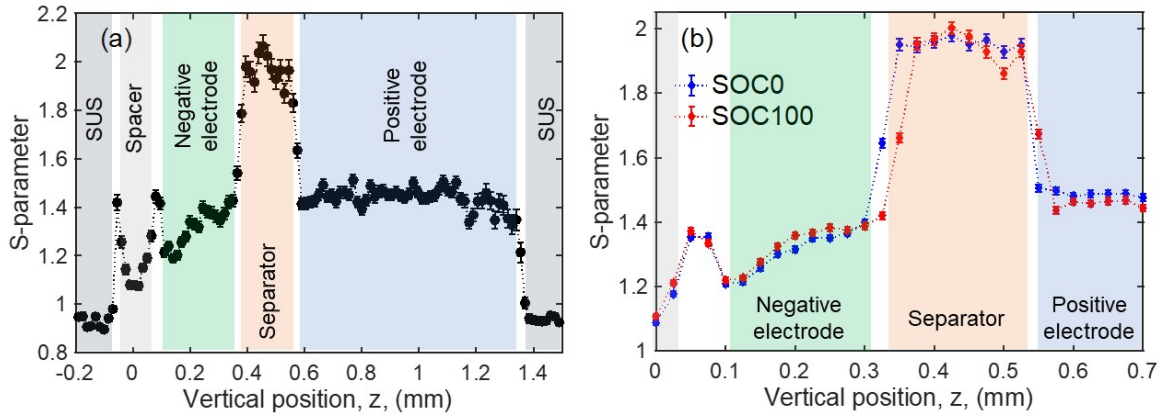

Figure 1. Internal Structure of the VL2020 coin cell observed by the *S*-parameters. (a) Components of the coin cell are distinguished by the value of *S*-parameters. (b) Change of *S*-parameters at positive and negative electrodes with the charge-discharge cycle displayed. Fully charged state (SOC100) and fully discharged state (SOC0) are shown in red and blue circles, respectively. The background color shows the regions of the corresponding components of the coin cell.

Lithium reaction distribution was obtained from two different charge-discharge rates of 0.2C and 1C, as shown in Figure 2. These distributions were obtained by scanning with the incident X-rays. The observing region on the coin cell is from the end of the negative electrode to the middle of the positive electrode, which is shown as a red square in Figure 2(a). The size of the total mapping region is 0.7 mm in height and 10 mm in width.

Preprints (www.preprints.org) | NOT PEER-REVIEWED | Posted: 23 August 2018 doi:10.20944/preprints201808.0413.v1

Peer-reviewed version available at Condens. Matter 2018, 3, 27; doi:10.3390/condmat3030027

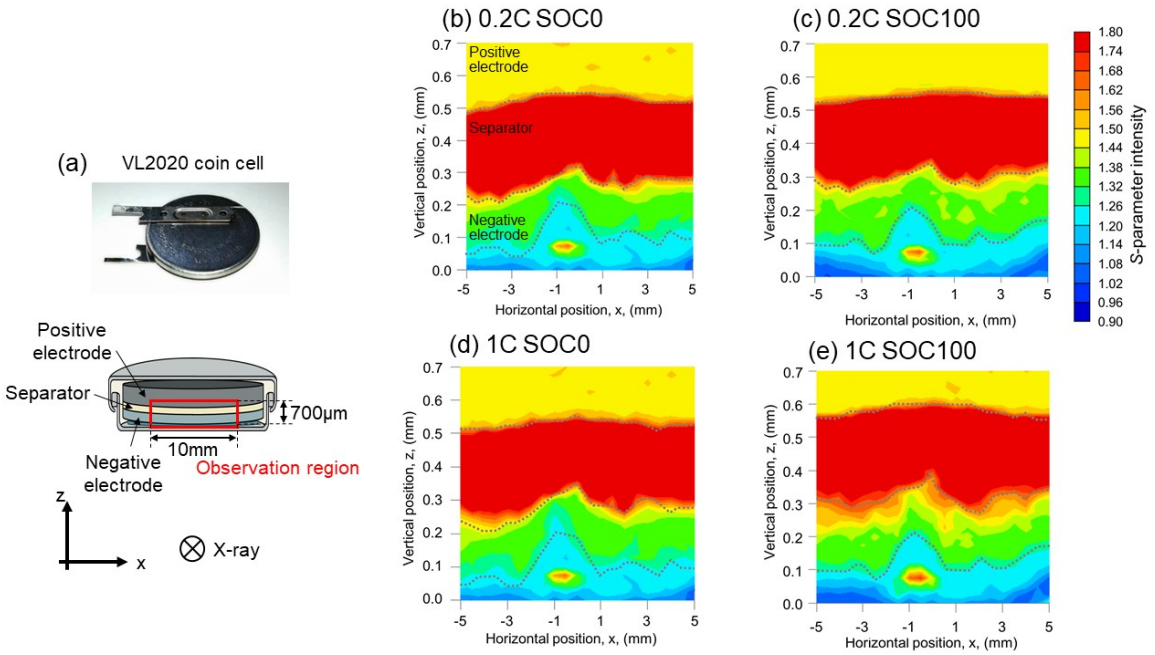

Figure 2. Lithium reaction distributions. (a) Picture of the sample and observation region of the lithium reaction distribution. (b) Lithium reaction distribution of fully discharged state obtained from the 0.2C rate. (c) Lithium reaction distribution of fully charged state obtained from 0.2C rate. (d) Lithium reaction distribution of fully discharged state obtained from the 1C rate. (e) Lithium reaction distribution of fully charged state obtained from the 1C rate. The color corresponds to the *S*-parameter intensity in these reaction maps.

Figures 2(b) and (c) correspond to SOC0 and SOC100 of lithium reaction distributions in the 0.2C rate, and Figures 2(d) and (e) correspond to SOC0 and SOC100 of lithium reaction distributions in the 1C rate. In Figures 2(b) and (d), the regions of high *S*-parameters are manifested at the region of the positive electrode; on the other hand, the regions of high *S*-parameters are manifested at the surface of the negative electrode in Figures 2(c) and (e). It is observed that the separator position moves toward the positive electrode direction when the battery is charged. Although this trend is the same in the 0.2C and 1C rates, the amount of movement of the separator at the 1C rate is larger than that of 0.2C rate. On the other hand, by discharging the battery, the separator position returns

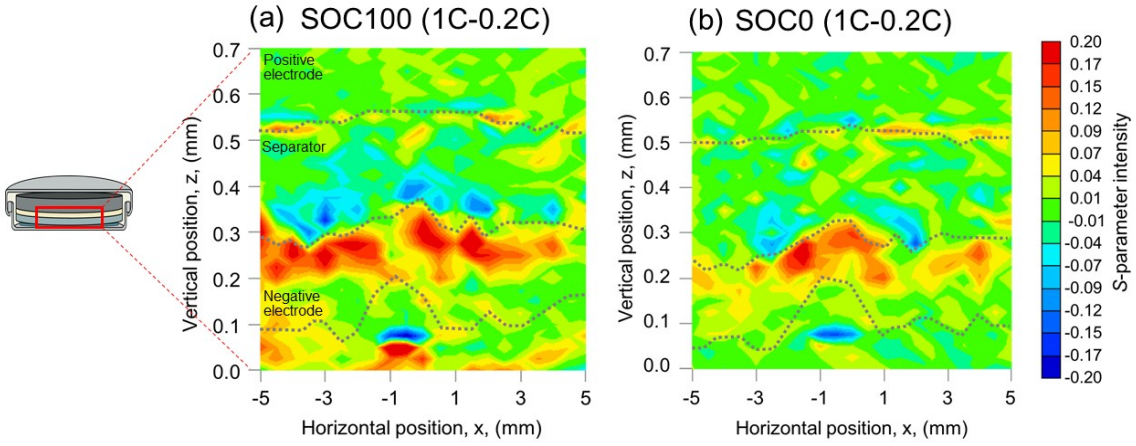

Figure 3. Change of lithium reaction distribution depending on charge-discharge rate, for 1C and 0.2C rates (a) At a fully charged state (SOC100). (b) At a fully discharged state (SOC0).

Preprints (www.preprints.org) | NOT PEER-REVIEWED | Posted: 23 August 2018 doi:10.20944/preprints201808.0413.v1

Peer-reviewed version available at Condens. Matter 2018, 3, 27; doi:10.3390/condmat3030027

to the initial position. This movement of the separator position corresponds to volume expansion or contraction of the electrode materials with moving lithium ions.

To exhibit the difference of lithium reaction distributions between 0.2C and 1C rates, we subtracted the lithium reaction distribution obtained at 1C rate from that obtained at 0.2C rate. Here, the separator position on lithium reaction distribution obtained at the 0.2C rate was corrected to agree with the separator position obtained at 1C rate following the same manner as previously reported [4]. Figures 3(a) and (b) correspond to the change of the distributions in the SOC100 and SOC0, respectively. In Figure 3(a), relatively vigorous lithium reactions occur at the surface of the negative electrode on the 1C rate. This trend of the lithium reactions occurring at the surface is the same as that reported previously in our study [4]. On the other hand, interestingly, when the battery was discharged by the 1C rate, as shown in Figure 3(b), high *S*-parameter values appeared around the horizontal position of x = -1 mm in the negative electrode. This means that the lithium ions remain into the negative electrode in the case of the 1C rate, although they move to the positive electrode on the full-discharged state of SOC0. These results were obtained by measuring nondestructively a commercial lithium-ion battery. Recently, the usage of lithium metal as a negative electrode material is considered to result in high-performance batteries, as the lithium metal has the highest theoretical capacity, 3861 mAh/g, among general negative electrode materials [13-15]. However, there is a problem that lithium dendrite occurs at the surface of the negative electrode. Our technique can be exploited to monitor the generation of lithium dendrite nondestructively.

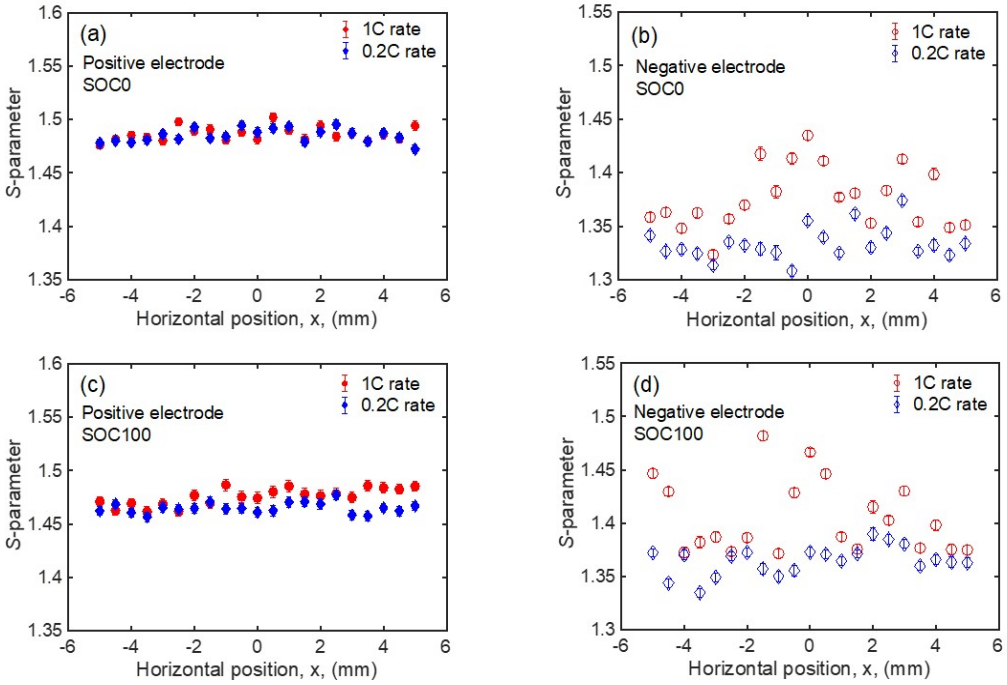

Figure 4. (a) *S*-parameters for each position at positive electrode in SOC0. (b) *S*-parameters for each position at negative electrode in SOC0. (c) *S*-parameters for each position at positive electrode in SOC100. (d) *S*-parameters for each position at negative electrode in SOC100. Blue and red symbols correspond to the results obtained from 0.2C and 1C rate, respectively.

Preprints (www.preprints.org) | NOT PEER-REVIEWED | Posted: 23 August 2018 doi:10.20944/preprints201808.0413.v1

Peer-reviewed version available at Condens. Matter 2018, 3, 27; doi:10.3390/condmat3030027

Table 1. Average values and deviations of *S*-parameters between 1C and 0.2C rates.

		Positive electrode		Negative electrode	
		SOC0	**SOC100**	**SOC0**	**SOC100**
1C rate	Average	1.486 ± 0.001	1.476 ± 0.001	1.376 ± 0.001	1.405 ± 0.001
	Deviation	0.006	0.008	0.028	0.033
0.2C rate	Average	1.485 ± 0.001	1.465 ± 0.001	1.334 ± 0.001	1.365 ± 0.001
	Deviation	0.006	0.005	0.015	0.013

In Figure 4, an average of the *S*-parameters is shown, which is obtained from Figure 2 for every horizontal position, x, in the coin cell at the positive and negative electrodes; Figures 4(a), (b), (c), and (d) correspond to the positive electrode at SOC0, the negative electrode at SOC0, the positive electrode at SOC100, and the negative electrode at SOC100, respectively. The average values and deviations of the *S*-parameters, obtained from Figure 4, are summarized in Table 1. In Figure 4 and Table 1, the *S*-parameters in the positive electrode are almost constant, regardless of charge-discharge speed. In contrast, the *S*-parameters in the negative electrode exhibit some variation. Deviation of the *S*-parameters at 1C rate is larger than that at 0.2C rate, and the value becomes almost two times higher. To discuss the inhomogeneity of the lithium distributions, the *S*-parameters were converted to lithium composition by using calibration curves between the *S*-parameter and lithium composition of positive and negative electrodes. The following calibration curves were used: $x_p = 32.476 \times S_p - 47.186$ for positive electrode and $x_n = 32.476 \times S_n - 47.186$ for negative electrode; x_p and x_n show the lithium compositions of $Li_xV_2O_5$ and Li_xAl, and S_p and S_n show the averaged *S*-parameters per horizontal position. In Figure 5, the lithium composition for every horizontal position, x, of the battery is shown; Figures 5(a), (b), (c), and (d) correspond to the positive electrode at SOC0, the negative electrode at SOC0, the positive electrode at SOC100, and the negative electrode at SOC100, respectively. The average values and deviations for the lithium composition are summarized in Table 2. In Figure 5 and Table 2, we confirmed that the deviation of the lithium composition obtained from the 1C rate is larger than that from the 0.2C rate.

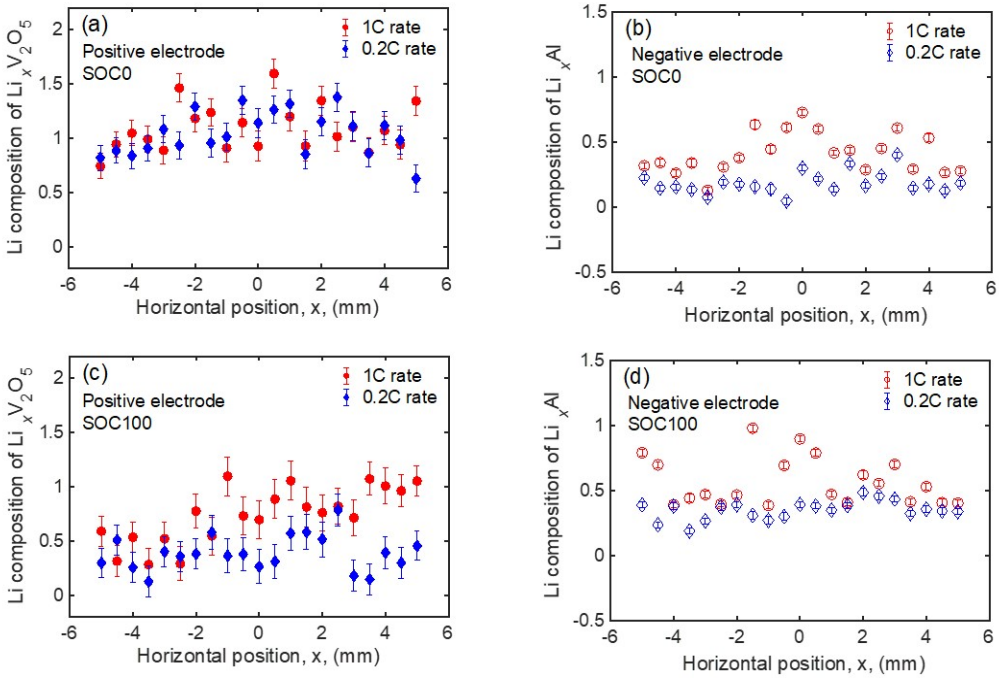

Figure 5. Lithium compositions of each position at (a) positive electrode in SOC0, (b) negative electrode in SOC0, (c) positive electrode in SOC100, (d) negative electrode in SOC100. Blue and red symbols correspond to the results obtained from the 0.2C and 1C rates, respectively.

Therefore, inhomogeneous reactions are promoted during high charge-discharge speed.

Table 2. Average values and deviations of lithium composition for the 1C and 0.2C rates.

		Positive electrode		Negative electrode	
		SOC0	**SOC100**	**SOC0**	**SOC100**
1C rate	Average	1.088 ± 0.028	0.738 ± 0.035	0.412 ± 0.005	0.566 ± 0.005
	Deviation	0.210	0.252	0.151	0.179
0.2C rate	Average	1.040 ± 0.028	0.387 ± 0.032	0.184 ± 0.005	0.349 ± 0.005
	Deviation	0.198	0.158	0.080	0.070

4. Conclusions

We applied the Compton scattering imaging technique for a commercial lithium coin cell. The motivation of this study is to deduce the charge-discharge rate dependency of lithium reaction distribution by directly monitoring lithium ions. This is directly linked with the safety and longevity of batteries. In this study, we observed the residual lithium ions at the center of negative electrodes on a fully discharged state by relatively high-speed discharge rate; the inhomogeneous reaction was facilitated on relatively high-speed charge-discharge rate, in both the negative and positive electrodes. Compton scattering imaging can also be applied to commercialized large-scale lithium-ion batteries and enable *in-situ* and *in-operando* measurements of the batteries. Therefore, the results are directly linked to the development of batteries products.

Author Contributions: Conceptualization, K.S., Y.S., and H.S. with suggestions from H.Y., Y.O., and Y.U.; Compton Scattering Experiment and Data Analysis, K.S., R.K., N.T., Y.S., and H.S.; Writing-Original Draft Preparation, K.S.; Writing-Review, all co-authors; Writing-Final Editing, K.S., N.T., Y.S., and H.S.; Funding Acquisition, K.S. and Y.S.

Funding: This project was funded by [Japan Science and Technology Agency] and [MEXT KAKENHI] grant number [15K17873].

Acknowledgments: We thank Dr. M. Itou for technical support of Compton scattering experiment. Compton scattering experiments were performed with the approval of JASRI [Proposal Nos. 2017A1123, 2017B1360 and 2018A1320].

Conflicts of Interest: The authors declare no conflict of interest.

References

1. Taminato, S.; Yonemura, M.; Shiotani, S.; Kamiyama, T.; Torii, S.; Nagao, M.; Ishikawa, Y.; Mori, K.; Fukunaga, T.; Onodera, Y.; Naka, T.; Morishima, M.; Ukyo, Y.; Adipranoto, D.S.; Arai, H.; Uchimoto, Y.; Ogumi, Z.; Suzuki, K.; Hirayama, M.; Kanno, R. Real-time observations of lithium battery reactions – operando neutron diffraction analysis during practical operation. *Sci. Rep.* **2016**, *6*, 28843, DOI 10.1038/srep28843.
2. Itou. M.; Orikasa, Y.; Gogyo, Y.; Suzuki, K.; Sakurai, H.; Uchimoto, Y.; Sakurai, Y. Compton scattering imaging of a working battery using synchrotron high-energy X-rays. *J. Synchrotron. Rad.* **2015**, *22*, 161-164, DOI 10.1107/S1600577514024321.
3. Suzuki, K.; Barbiellini, B.; Orikasa, Y.; Kaprzyk, S.; Itou, M.; Yamamoto, K.; Wang, Y.J.; Hafiz, H.; Uchimoto, Y.; Bansil, A.; Sakurai, Y.; Sakurai, H. Non-destructive measurement of in-operando lithium concentration in batteries via x-ray Compton scattering. *J. Appl. Phys.* **2016**, *119*, 025103, DOI 10.1063/1.4939304.
4. Suzuki, K.; Suzuki, A.; Ishikawa, T.; Itou, M.; Yamashige, H.; Orikasa, Y.; Uchimoto, Y.; Sakurai, Y.; Sakurai, H. In-operando quantitation of Li concentration for commercial Li-ion rechargeable battery using high-energy X-ray Compton scattering. *J. Synchrotron. Rad.* **2017**, *24*, 1006, DOI 10.1107/S1600577517010098.

5. Harding, H.; Harding, E. Compton scatter imaging: A tool for historical exploration. *Appl. Rad. Isotope.* **2010**, 68, 993-1005, DOI 10.1016/j.apradiso.2010.01.035.
6. Schülke, W. The theory of Compton scattering. In *X-ray Compton Scattering*, 1st ed.; Cooper, M.J., Mijnarends, P.E., Shiotani, N., Sakai, N., Bansil, A., Eds.; Oxford University Press: Oxford, UK, 2004; pp. 22–81, ISBN 978-0-19-850168-8.
7. Barbiellini, B. A natural orbital method for the electron momentum distribution in mater. *J. Phys. Chem. Solids* **2000**, *61*, 341-344, DOI 10.1016/S0022-3697(99)00313-3.
8. Barbiellini, B.; Bansil, A. Treatment of correlation effects in electron momentum density: density functional theory and beyond. *J. Phys. Chem. Solids* **2001**, *62*, 2181-2189, DOI 10.1016/S0022-3697(01)00176-7.
9. Suzuki, K.; Barbiellini, B.; Orikasa, Y.; Go, N.; Sakurai, H.; Kaprzyk, S.; Itou, M.; Yamamoto, K.; Uchimoto, Y.; Wang, Y.J.; Hafiz, H.; Bansil, A.; Sakurai, Y. Extracting the redox orbitals in Li battery materials with high-resolution X-ray Compton scattering spectroscopy. *Phys. Rev. Lett.* **2015**, *114*, 087401, DOI 10.1103/PhysRevLett.114.087401.
10. Barbiellini, B.; Suzuki, K.; Orikasa, Y.; Kaprzyk, S.; Itou, M.; Yamamoto, K.; Wang, Y.J.; Hafiz, H.; Yamada, R.; Uchimoto, Y.; Bansil, A.; Sakurai, Y.; Sakurai, H. Identifying a descriptor for d-orbital delocalization in cathodes of Li batteries based on x-ray Compton scattering. *Appl. Phys. Lett.* **2016**, *109*, 073102, DOI 10.1063/1.4961055.
11. Hafiz, H.; Suzuki, K.; Barbiellini. B.; Orikasa, Y.; Callewaert, V.; Kaprzyk, S.; Itou, M.; Yamamoto, K.; Yamada, R.; Uchimoto, Y.; Sakurai, Y.; Sakurai, H.; Bansil, A. Visualizing redox orbitals and their potentials in advanced lithium-ion battery materials using high-resolution X-ray Compton scattering. *Sci. Adv.* **2017**, *3*, e1700971, DOI 10.1126/sciadv.1700971.
12. Biggs, F.; Mendelsohn, L.B.; Mann, J.B. Hartree-Fock Compton profiles for the elements. *At. Data Nucl. Data Tables*. **1975**, 16, 201.
13. Wang, X.; Hou, Y.; Zhu, Y.; Wu, Y.; Holze, R. An aqueous rechargeable lithium battery using coated Li metal as anode. *Sci. Rep.* **2013**, *3*, 1401, DOI 10.1038/srep01401.
14. Younesi, R.; Veith, G.M.; Johansson, P.; Edström, K.; Vegge, T. Lithium salts for advanced lithium batteries: Li-metal, Li-O_2, and Li-S. *Energy Environ. Sci.* **2015**, *8*, 1905, DOI 10.1039/c5ee01215e.
15. Zhang, X.Q.; Cheng, X.B.; Zhang, Q. Advances in interfaces between Li metal anode and electrolyte. *Adv. Mater. Interfaces*. **2018**, 5, 1701097, DOI 10.1002/admi.201701097.